

A DEEP MULTICOLOR SURVEY I. IMAGING OBSERVATIONS AND CATALOG OF STELLAR OBJECTS

Patrick B. Hall¹

Steward Observatory, University of Arizona, Tucson AZ 85721

E-mail: phall@as.arizona.edu

Patrick S. Osmer

Astronomy Department, The Ohio State University, 174 West 18th Avenue, Columbus, OH 43210

E-mail: posmer@payne.mps.ohio-state.edu

Richard F. Green, Alain C. Porter²

National Optical Astronomy Observatories, P.O. Box 26732, Tucson AZ 85726

E-mail: rgreen@noao.edu

Stephen J. Warren

Imperial College, Astrophysics Group, The Blackett Laboratory, Prince Consort Road, London SW7 2BZ

E-mail: s.j.warren@ic.ac.uk

Subject headings: Surveys, Quasars: General, Stars: General, Galaxies: General

ABSTRACT

We have used the KPNO 4-meter Mayall telescope to image 0.83 square degrees of sky in six fields at high galactic latitude in six filters spanning 3000-10000Å to magnitude limits ranging from 22.1 to 23.8. We have assembled a catalog of 21,375 stellar objects detected in the fields for use primarily in conducting a multicolor search for quasars. This paper describes the data reduction techniques used on the CCD data, the methods used to construct the stellar object catalog, and the simulations performed to understand its completeness and contamination.

¹Visiting Student, Kitt Peak National Observatory, National Optical Astronomy Observatories, operated by AURA Inc., under contract with the National Science Foundation.

²Deceased.

1. Introduction

Quasars, thought to be powered by the accretion of matter onto supermassive ($\sim 10^7-10^8 M_\odot$) black holes at the centers of galaxies, are the most luminous individual objects in the universe ($-31 < M < -23$). As such, they can be seen to greater distances than any other objects, providing us with a unique opportunity to study the universe back to times when it was only $\sim 10\%$ of its current age. Quasars yield information about the universe through their absorption-line systems and associated galaxies (e.g. Steidel & Sargent 1992), through the galaxies in quasar environments (Yee & Ellingson 1993, and references therein), and through the lensing of quasars by intervening systems (Kaiser & Tribble 1991), to name but a few. Additionally, the mere existence of quasars at the observed space densities at redshifts $z > 4$, when the universe was only $\sim 10\%$ of its current age, constrains models of galaxy and structure formation in the universe (e.g. Turner 1991, Loeb 1993, Nusser & Silk 1993, Haehnelt & Rees 1993, Katz et al. 1994).

One direct way of using quasars to study the universe is to map the evolution of the quasar luminosity function (QLF) with lookback time; that is, the number of quasars as a function of absolute magnitude and redshift (e.g., Schmidt & Green 1983, Hewett et al. 1993). Previous studies of the QLF have shown that the space density of the bulk of the quasar population, with $-28 < M < -23$, was considerably greater in the past, by a factor of ~ 100 at $z=2$ relative to the current comoving density. This was likely due to the evolution of the quasar population in both luminosity and in density, though the exact form of the evolution is not well constrained (Hewett et al. 1993). The redshift distribution of these quasars may peak at $z \sim 2-3$ and decrease at $z > 3$, though not as swiftly as at $z < 2$, as first proposed by Osmer (1982).

Recently Warren, Hewett, & Osmer (1994; hereafter WHO), using a multicolor-selected sam-

ple of 86 quasars with $2.2 < z < 4.5$, showed that there is indeed a decline in the observed space density of quasars with $z > 3$. This conclusion has been confirmed by the recent results of Schmidt, Schneider, & Gunn (1995), using a $\text{Ly}\alpha$ -selected sample of 90 quasars with $2.75 < z < 4.75$. Although some groups have previously found no evidence for such a decline (e.g. Koo & Kron 1988 (KK88), Giallongo & Vagnetti 1992), these more recent studies argue that the decline is real. However, it should be noted that WHO cannot rule out that the decline they see in the *observed* quasar space density at $z > 3$ is due to dust obscuration, as suggested by e.g. Fall & Pei (1993), and not reflective of a decrease in the *true* space density of quasars at high redshift. One of the reasons for this contention over the behavior of the QLF at high redshift is that each sample of quasars typically contains only a few such objects. In addition, accurate determination of the space density of quasars at high redshift requires careful modelling of the selection effects present in each survey in order to make incompleteness corrections, as discussed e.g. in Warren et al. (1991a).

There is obviously a need for additional carefully-selected samples of quasars with $z > 2.2$. In 1990 we initiated a deep multicolor survey for quasars with the intent of obtaining such a sample. Our survey was enabled by the arrival of the first 2048×2048 CCD at the KPNO 4-m telescope; the detector and telescope offered at that time a unique combination of large areal coverage on the sky, spectral sensitivity across the optical band, and deep limiting magnitude. The survey was conducted in six optical filters spanning $3000-9000\text{\AA}$ in six different high-Galactic-latitude fields. The primary objective was to construct a well-defined stellar locus from which quasar candidates could be easily isolated via their unusual colors. However, many other interesting questions can be addressed with the survey. We achieved good photometric calibration and the star-galaxy classification effects are

well understood, and thus the survey should be useful for studies of Galactic star counts (Reid & Majewski 1993). The large number of galaxies detected in the survey also forms a valuable database for the study of field and emission-line galaxies. Our wide wavelength coverage makes the survey especially useful for studies of field galaxy color evolution and for the identification of rare galaxy types such as E+A galaxies (Liu et al. 1996).

Quasars with $-25 < M < -23$ at $z=3-5$ are found at apparent magnitudes of roughly $20 < R < 23$, so our goal was to image to $R=24$ ($R=23.5$ was achieved). Such a faint limiting magnitude also probes the upper end of the Seyfert luminosity function at $z < 3$. To our limiting magnitudes, the survey region contains approximately 30,000 objects, of which about half are galaxies. Based on previous knowledge of the apparent luminosity function of quasars (Majewski et al. 1993), it should contain almost 200 quasars. Our ultimate goal is to make available catalogs of the quasars, galaxies, and stars containing accurate positions, magnitudes, and photometric error estimates for all the objects.

The survey for quasars had two principal objectives: 1) to investigate the luminosity function of high-redshift quasars ($z > 3$) at fainter magnitudes than had been done before, for which the absolute magnitudes were more comparable with previous surveys at lower redshift; and 2) to determine the luminosity function of quasars with $z \leq 2.2$ at faint enough magnitudes to constrain the debate on luminosity vs. density evolution, which has been unresolved for lack of data at the faint end of the luminosity function, where the differences between the two hypotheses are pronounced.

This paper describes the CCD imaging observations done for the survey and the data reduction methods used to construct the catalog of stellar objects from which quasar candidates were chosen. (We define a *stellar object* as an object detected in our images that is found by

our classification routines to have an appearance consistent with an unresolved point source in a certain minimum number of images, as detailed in §4.3 below.) Paper II (Hall et al. 1996) discusses quasar candidate selection and initial spectroscopic results, and makes a comparison with expectations from previous luminosity function studies. Paper III (Osmer et al. 1996) will present final spectroscopic results and a detailed derivation of the luminosity function.

This paper is organized as follows. In §2 we describe the observations, the survey fields, and the filters used. We cover in §3 the main features of the data reduction steps. In §4 we summarize how objects were detected and cataloged using FOCAS and how the photometric measurements were made. We discuss in §5 the photometric calibration and analysis of the errors, and in §6 the astrometric calibrations. Finally, in §7 we summarize the properties of the resulting catalog of stellar objects.

2. Observations

Images were obtained at the prime focus (f/2.7) of the KPNO 4-meter Mayall telescope with a Tektronix 2048x2048 CCD with 27-micron pixels, giving a plate scale of $0''.529/\text{pixel}$. A gain of 11 e-/ADU was used, yielding a full well of $\sim 30,000$ ADU. The particular CCD we used was an engineering grade, thick chip with poor cosmetics. It had a useful area of 1860x2048 pixels due to an excess of variable bad columns on one side of the chip, and also had a large number of traps evident in the lower light levels of the UBV images.

We used a set of six filters covering the wavelength range from 3000 to 9000 Å. The set consisted of standard KPNO Johnson UBV filters ($\lambda_{eff} = 3595$ Å, 4364 Å, and 5563 Å respectively) plus three special red/near-IR filters: R', I75, and I86 ($\lambda_{eff} = 6615$ Å, 7425 Å, and 8586 Å respectively). The response curves for each filter in the absence of atmospheric extinction are plot-

ted in Figure 1. Each curve is the product of the quantum efficiency of the CCD, the transmission of the filter, the transmission of the 4-meter prime focus doublet corrector, and one reflection off aluminum. The R' filter is narrower than the standard KPNO Harris (not Mould) R filter, having less of a red tail and also being less transmissive overall, but it has very nearly the same effective wavelength (6615 Å) as the standard KPNO Harris R filter (6625 Å). Thus for most objects it is safe to treat magnitudes in this filter as a standard Harris R filter; only the zero-point of the photometric solution will differ substantially from the solution for a Harris R filter (although there will be a color term for very red objects). Hereafter the R' filter will be referred to simply as R. The I75 and I86 filters each cover about half the wavelength range of the standard I filter. These three red filters were designed with narrower than usual bandpasses in order to improve our ability to detect quasars with redshifts as large as 5.5 and to distinguish $z > 4$ quasars from very late-type stars via the strong excess from $L\alpha$ emission. For $z \leq 5.5$, the I86 filter is still longward of redshifted $L\alpha$ emission, which is normally the strongest line in quasar spectra, and therefore provides a discriminant between high- z quasars and later-type stars.

Successful imaging runs, affected only occasionally by light cirrus, were carried out on 1990 August 21-24 and 1991 April 14-17, resulting in images being obtained in twelve CCD fields. Our fields are arranged on the sky in six pairs of two adjacent individual CCD fields (with slight overlaps), and were chosen to be at high galactic latitude away from known dust clouds. A list of the coordinates, area, and galactic extinction parameters for each field is given in Table 1.

We attempted to obtain two sky-noise-limited images of each field in every filter, offset by typically ten arcseconds from each other, to help reduce spurious detections of cosmic ray hits and bad pixels. We succeeded in obtaining at least two offset images except in the 01e field and the

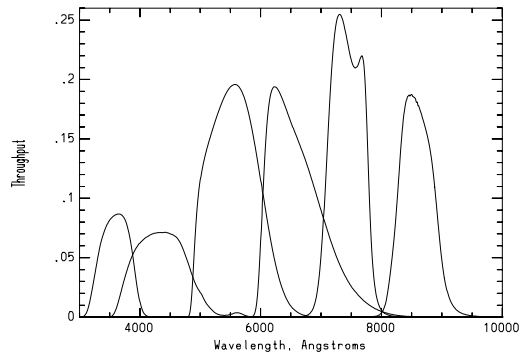


Fig. 1.— The response curves of the survey in each filter (UBVRI75I86 from left to right). Each curve is the product of the quantum efficiency of the CCD, the transmission of the filter, the transmission of the 4-meter prime focus doublet corrector, and one reflection off aluminum. Atmospheric extinction has not been figured into these curves.

10e field in the B filter. Where more than two offset images were obtained, the two best in terms of seeing, depth, and focus quality across the chip were selected to be the final two images used in the reduction process. Various parameters of these 125 CCD images that comprise the survey are listed in Table 2.

3. Data Reduction

The CCD images in all filters of each field were reduced using IRAF³. The bias level was subtracted from each column separately on all field, dark, and domeflat images. The appropriate dark current image was subtracted from each field image, and domeflats were used to remove the pixel-to-pixel sensitivity variations. A separate bad pixel mask needed to be made for each image. Each bad area was interpolated across its narrowest dimension.

³The Image Reduction and Analysis Facility (IRAF) is distributed by the National Optical Astronomy Observatories, which is operated by AURA, Inc., under contract to the National Science Foundation.

It was found at this point that the images still showed random, nonrepeatable gradients and variations in the sky level across the chip. This was particularly true in the three reddest bands, where the variations were typically 5% peak-to-peak. These variations were assumed to be random additive variations in the sky values, and were removed using a two-step process. First, all images in a particular filter for each run were combined to form a “skyflat” (identical to the “supersky” described in Gullixson 1992) using a program supplied by Todd Boroson. The images were scaled by the mode of a central region and then median filtered to form the skyflat. This procedure was successful at eliminating objects completely except when fewer than 10 images were available to form the median. To eliminate artifacts from such residuals, we smoothed the skyflat using a variably sized boxcar filter via the IRAF MKSKYCOR task. Each skyflat was then normalized by the mode of its central area and divided into the images, resulting in a reduction of the gradients and variations across each image to at most the 2% level. To eliminate these remaining random variations, which could be found in every filter except U, we used the Faint Object Classification and Analysis System (FOCAS, Valdes 1982a) sky-fitting routine to estimate the local sky value for every 8x8 pixel box. The sky values determined by FOCAS were found to be accurate to within 1% even in areas dominated by saturated stars, but were offset from their true locations slightly due to the line-by-line process of sky determination used by FOCAS. To avoid creating troughs to one side of bright objects after sky subtraction, we produced three additional FOCAS sky images, rotating the image by 90° between each. These sky images were rotated back to the original orientation and medianed with the first sky image, discarding the highest pixel, to form the final sky image. Each field image had its own sky image subtracted from it, leaving fields globally flat to <0.5%. The only shortcoming of this method was that the outer regions of the

largest, most extended galaxies present (typically 20–50'' in size) were sometimes confused with the sky, resulting in an oversubtraction of the sky around these galaxies. This effect is not of concern for the catalog of stellar objects.

Next, cosmic rays were isolated and interpolated across using the IRAF task COSMICRAYS. The removal worked quite well, having trouble only with some many-pixel cosmic ray hits and almost never flagging unsaturated objects by mistake. To allow us to be conservative in our eventual selection of candidates in the event that the interpolation introduced errors into the object photometry, all cosmic ray locations were added to the bad pixel lists for later cross-correlation with the object lists.

Lastly, the images were shifted and trimmed so that each CCD field was on a common coordinate system to the nearest pixel (no fractional pixel shifts were used). The area covered by these trimmed images, taking into account the additional reduction from adjacent field overlaps and the 5'' wide border on each image unused by FOCAS, is given in Table 1. The total areal coverage on the sky of the survey is $2990\Box'$, or $0.83\Box^\circ$.

4. Detection and Cataloguing of Objects

Because of the variations in seeing, focus, and pointing between the two images in each filter in our fields (which were often taken on different nights), as well as the problem of cosmic-ray contamination, we decided not to coadd the images to produce a single image with improved signal-to-noise (S/N) in each filter. Instead, we reduced each frame individually and improved the S/N by averaging the magnitudes from each frame after they had been reduced. The main drawback to this approach with respect to coadding is the increased unreliability of object classification at faint magnitudes, but we are helped in this by having two independent classifications. We used FOCAS and its ‘built-in’ detection filter to detect and classify all the objects in our frames, and the

IRAF PHOT routine to find aperture magnitudes for them.

A brief summary of the detection and initial photometry steps performed on each field follows:

- FOCAS detections must have at least 9 contiguous pixels 2.5σ above the sky, after the value of each pixel was convolved with the values of pixels within a 5×5 grid, weighted according to the standard ‘built-in’ FOCAS detection filter
- Objects lying on bad pixels were flagged as such
- Objects were classified using a different empirical PSF for each of nine subsections on each image
- Objects not appearing on both images in the filter were discarded
- To be considered stellar in appearance, objects were required to be classified as a star in at least one image of half or more of the filters in which they were detected
- Aperture corrections were calculated for each image subsection
- Instrumental magnitudes were calculated in a $3''.0$ diameter aperture
- The instrumental magnitudes were calibrated to a standard system
- Magnitudes from each image in each filter were combined, accounting for bad pixel contamination and magnitude limits, to give a final magnitude for each object.

Below, we discuss important reduction steps in more detail, where necessary.

4.1. Bad Pixels

All objects that fell on bad pixels were flagged as such. ‘Bad pixel’ here is a broad term, including sites of detected cosmic ray hits, the actual bad columns and traps determined through inspection, and the bad focus regions (typically the corners) of each image. Saturated stars were also considered to fall on bad pixel areas, but were flagged differently since the determination of color limits for such objects is different than

for regular bad pixels (we measure a lower limit to the object’s magnitude in these cases).

4.2. Classification

Objects were classified using the standard FOCAS method and parameters, using the resolution classifier fully described in Valdes (1982b) and summarized briefly here. An empirical point-spread function (PSF) is constructed from isolated bright stars. From the PSF a set of classification templates is generated, consisting basically of a broadened or narrowed PSF. Objects were then classified as star, fuzzy star, galaxy, diffuse object, or noise spike depending on which template they best fitted. Due to the frequent variation in focus across the chip, each image was divided into 9 subsections in a 3×3 grid, and a different empirical PSF was used for classification in each subsection. This method is obviously not as accurate as fitting a slowly varying PSF across the chip; but the latter method is difficult to implement with FOCAS. We included ‘fuzzy stars’ in our stellar object list to increase our ability to include objects where an active nucleus is seen along with extended light from a host, companion, or intervening galaxy. Inspection of the location of objects on a plot of PSF scale vs. nuclear component fraction showed that only $\sim 10\%$ of fuzzy stars have an extended component with amplitude significantly different from zero. This tells us that extended objects with strong nuclear light components are relatively rare, and reassures us that we are not including a large number of galaxies with this criterion.

It should be noted that some of the frames had a strong gradient in focus across them, causing substantially out of focus images at the corners of the chip. Objects in these regions were flagged so that the photometry from them is not used; fortunately, no region was out of focus in both offset images of the field.

4.3. The Stellar Object Catalog: Selection, Completeness, and Misclassification

Both offset frames in each filter were matched with each other, and objects not detected in both offset images were discarded. An object was classified stellar *in a given filter* if it was classified by FOCAS as a star or fuzzy star in *either* offset frame of the filter. The criteria for inclusion in the final catalog of stellar objects were that the object be detected in at least three filters and classified as stellar in half or more of the filters in which it was detected. Our criteria are rather lenient in allowing objects classified as nonstellar in some images to be included in the stellar object catalog because we did not want to exclude faint AGN with detectable host galaxies. We need to understand how often nonstellar objects are misclassified as stellar, and vice versa, as a function of magnitude in each filter in order to understand the contamination and completeness of our catalog.

The ideal method of determining the completeness and classification reliability is to add to the original images simulated objects of known morphology and a wide range of magnitude. These images are then processed as the original images were, and the completeness and classification reliability are straightforward to determine. However, the varying PSF over many of our CCD images makes the addition of accurately simulated objects to the data complicated. Instead, we opted to create entirely artificial images and analyze them. Since the parameters of the artificial data can be made to match those of the real data very accurately, this approach should yield an accurate description of the real data's classification reliability and completeness as a function of magnitude.

We used the IRAF ARTDATA package to simulate two images of a CCD field in each filter. We attempted to match the seeing, background, and noise level observed in the 01w field. For the

galaxies, to subjectively match the appearance of the real data, a characteristic radius of 5.3" and a mixture of 40% de Vaucouleurs profile 'bulges' and 60% exponential profile 'disks' was chosen. Galaxies were given a power-law magnitude distribution with slope 0.35 (i.e. $n(m) \sim 10^{0.35m}$), which matches well the slope of faint magnitude galaxy counts. To increase the number of faint stars available for studying completeness, stars were given a power-law magnitude distribution with slope 0.6, steeper than the observed distribution. However, since this distribution does not generate as many bright stars as the real images contain, it was necessary to add a grid of bright stars to the images to ensure that the PSF could be well determined in each image subsection. Since whether or not an object is included in our catalog of stellar objects depends on its classification and magnitude in several filters, objects of different colors had to be simulated. We divided the locus of stellar objects in our real data into five bins, each with different broadband colors. The relative numbers of stars and galaxies in each bin was determined from the real data, and corresponding percentages of the simulated stars and galaxies were assigned the colors of each bin. Finally, following the above parameters, 3000 stars and 2500 galaxies with $R=16-24$ were randomly distributed across the field. The appearance and statistics of the images closely matched those of the real data. One minor difference is that the PSF in the real data is not a perfect gaussian. However, the difference between the real PSF and the simulated one is only apparent in the wings of bright stellar objects, and so this difference should not affect any of our results on faint objects.

Our detection and cataloging programs were then run on the artificial images in exactly the same manner as on the real data, producing an output FOCAS catalog of stellar objects. The FOCAS task ARTCAT was used to create FOCAS catalogs of the stars and galaxies input to the ARTDATA task, for comparison with the output cata-

log.

To determine its completeness, the output catalog of stellar objects was compared to the input catalog of stars. As is typical for CCD data (Stetson 1990), the completeness fraction is 100% at bright magnitudes, begins a slow linear decline at some faint threshold magnitude as the effects of crowding appear, and then switches to a rapid linear decline as the detection threshold comes to dominate over crowding effects. We find that this transition occurs at about the 90% completeness level, which closely approximates the 5σ detection limit (see §4.5). Similarly, the 50% completeness limit closely approximates the 3σ detection limit. These limits are listed in Table 3, along with the threshold magnitude above which the completeness is essentially 100%.

To determine the classification reliability, the output catalog of stellar objects was compared to the input catalog of galaxies to determine which supposedly stellar objects were actually misclassified galaxies. In principle, false detections due to noise could also show up in the catalog, but by requiring detection in both offset frames of at least three filters we completely eliminate such detections. 376 galaxies were misclassified as stars in our simulations, virtually none of them brighter than the completeness threshold magnitude, which we thus adopt as the threshold magnitude for classification as well. To apply these results to the real dataset requires adjusting for the expected number of faint galaxies in the survey fields versus the number used in the simulated data, since the number of misclassified galaxies in the catalog obviously depends on the number of galaxies that exist in our fields. We used the compilation of McLeod & Rieke (1995) to determine the number of faint galaxies expected in our fields as a function of magnitude. The slope of the $N(m)$ relation for our simulated galaxies is 0.35, close enough to the value observed for faint optical counts that we only need to adjust the normalization. To approximate the counts from $R=21.5$ – 23.5 we used

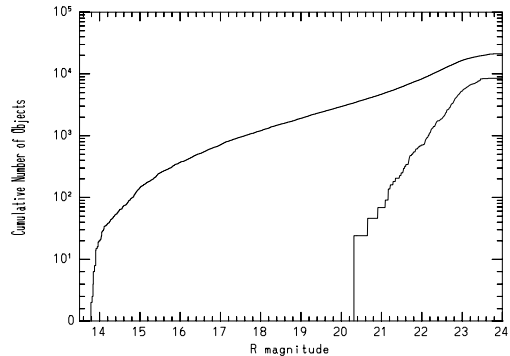


Fig. 2.— The upper curve is the observed cumulative number-magnitude (R band) counts of all 21375 objects in the stellar object catalog. The lower curve is the expected cumulative number-magnitude (R band) distribution of misclassified galaxies in the catalog, based on scaling the results of the artificial data simulations described in the text to the expected galaxy number density and total area of the survey. At faint magnitudes ($R \gtrsim 21.5$) the stellar object catalog shows an excess above the power-law distribution seen at intermediate magnitudes, which may reasonably be attributed to misclassified galaxies.

the counts from Gunn $r=22$ – 24 and assumed that those counts are 100% complete. In our 0.0713° simulated field, the input catalog contained 1761 galaxies from $R=21.5$ – 23.5 , whereas $\sim 50\%$ more (2797) are expected in an equal area of real data. Thus to make our simulated field accurately reflect the number density of faint galaxies, we adjust the total number of contaminating galaxies upwards by 50%, from 376 to 564. In our entire survey area of 0.83° , we then expect 6565 spurious objects in the stellar object catalog.

Using this scaling and the magnitude distribution of the misclassified galaxies in our simulation, in Figure 2 we compare (in the R band) the expected number of contaminating galaxies to the total number-magnitude counts of the stellar object catalog. At faint magnitudes ($R \gtrsim 21.5$) the stellar object catalog shows an excess above

the power-law distribution seen at intermediate magnitudes. This may reasonably be attributed to misclassified galaxies. A further 30% increase in the number of contaminating galaxies, to 8535, is required to provide a good match to the number-magnitude distribution of this excess.

What might have caused our simulations to underpredict the number of misclassified galaxies? There are some effects we have neglected in the simulations, but most of them should not alter our conclusions significantly:

- We have not included cosmic rays in the artificial data, although this capability does exist within ARTDATA. Cosmic rays would effectively act as another source of noise, and since our selection criteria are very efficient at keeping false detections due to noise out of the catalog, their effect is negligible.
- We have not included the effects of interpolating over bad pixels, although this is not difficult to do either. Interpolation might cause objects to fall below the detection threshold or be misclassified. Since the area affected by bad pixels is very small and its location varies from image to image, and since our criteria for inclusion in the final catalog uses information from many images, the effect of bad pixels should be negligible.
- We have ignored the effects of galaxy clustering, since its amplitude is very weak at these magnitudes (Neuschaefer & Windhorst 1995, Roche et al. 1993).
- In reality, different fields have different values for the seeing, galaxy and star number counts, etc., than those used in the simulated data. However, the 01w field that we simulated is fairly typical in these respects, so generalizing the results of the simulated 01w data to the entire survey should be valid.
- We have not taken into account that one of our fields, the 01e field, has only one offset image in each filter, so that its completeness and contamination properties will be different than

those of the other fields. This will likely raise the contamination fraction and possibly reduce the completeness slightly, but since the area affected is <10% of the total the effect should be negligible.

- One possibly significant effect not included is the variable PSF over many of our images, due mostly to a softening of the focus at increasing distances from the center of the field. This will in general have the effect of increasing the contamination, since the classification of faint objects is more difficult when the PSF is broader. However, only a small fraction of the total area of the survey has an extremely broad PSF, so its effects should not greatly alter the conclusions of our simulations.

The most important potential problem with our simulations is the scale radii used for the simulated galaxies in them. Recent results from the *HST* Medium Deep Survey (MDS; Griffiths et al. 1994, Im et al. 1995) suggest that many faint galaxies have very small half-light radii (median $0''.4$ at $V=21-24$). Naturally, galaxies with small scale radii are more easily misclassified as stars than galaxies with large scale radii under any seeing conditions. Our simulated galaxies have half-light radii from $0''.5-1''.5$ at faint magnitudes; thus, we may have underestimated the contamination fraction in the stellar object catalog. Based on the fraction of our simulated galaxies misclassified as stars as a function of their scale radii, we estimate that using the MDS scale radii distribution would lead to a doubling of the contamination fraction in the stellar object catalog. The contamination fraction is also dependent, albeit to a lesser degree, upon the relative numbers of galaxies with de Vaucouleurs and exponential profiles, and the inclination angle distribution of the latter population. However, these are second-order effects, and our chosen values for the parameters involved should be valid for all but the faintest magnitudes (cf. Im et al. 1995).

The MDS results are preliminary, being based

on a small number of galaxies; also, due to the small area studied so far, there is very little data on the distribution of galaxy scale radii at brighter magnitudes. It is thus perhaps not surprising that results from the Canada-France Redshift Survey show that only 1% of all galaxies at $17.5 < I_{AB} < 22.5$ ($\sim 19.5 < B < 24.5$) are as compact as stars on images with $0''.9$ seeing (Crampton et al. 1995). While our seeing is rarely that good, this result indicates that the distribution of galaxy scale radii used in the simulations may not be as unrealistic as the MDS results suggest, particularly at brighter magnitudes. In the next few years more extensive data from the MDS should yield very accurate distributions of galaxy scale radii, morphological types, and axis ratios over a large magnitude range. This will enable more accurate simulations to be done to help understand the results of ground-based imaging. Based on the preliminary MDS results, we feel that an upwards adjustment of 30% in the contamination fraction of the stellar object catalog is reasonable. (Recall that this adjustment results in a excellent fit to the observed excess of faint stellar objects above an extrapolation of the counts at brighter magnitudes.)

Thus, in summary, we adopt as the total contamination fraction of our catalog the prediction of our simulated data, scaled to the expected number density of faint galaxies and the size of our survey, then adjusted upwards by 30%. Since the catalog contains 21375 objects, its overall contamination fraction is 40% (8535 objects), with roughly half of that occurring fainter than the 5σ limit. We parametrize the integral contamination in each filter (i.e. the total number of misclassified galaxies in the catalog brighter than a given magnitude in that filter) as a cubic function rising from zero at the threshold magnitude to its maximum value at the 3σ limiting magnitude. These magnitudes are tabulated for each filter in Table 3, along with the integral contamination at the 5σ limiting magnitude. The completeness of the catalog in each filter

is 100% down to the threshold magnitude and then declines linearly to 90% at the 5σ limiting magnitude and 50% at the 3σ limiting magnitude. The contamination ($\sim 25\%$) and completeness (90%) of the stellar object catalog at the 5σ limits are well characterized and allow for reliable corrections to be made when computing number counts, etc.

4.4. Photometry and Aperture Corrections

Aperture photometry of all stellar objects was performed with the IRAF PHOT task, using a centroiding algorithm to determine the position of the aperture center. The instrumental magnitudes were calculated using a 3-pixel ($1''.6$) radius circular aperture and a sky annulus $2''.7$ wide $8''$ away. This was found to be the best compromise between maximizing the enclosed signal and reducing the scatter between different measurements of the same object due to focus and seeing variations between different exposures. Aperture photometry was performed at the object's estimated coordinates in all filters, even if the object had not been originally detected in the particular filter, in order to obtain color limits on such objects. In such cases, occasional centering errors would occur and need to be corrected — the centering routine would latch on to a nearby object or noise spike and center the aperture in that position, rather than the object's expected position.

Aperture corrections were used to correct the magnitude measured in a $1''.6$ aperture to the $5''.8$ aperture used for the standard stars. The corrections were interactively calculated for the 9 subsections on each image separately, using up to 20 of the brightest stars in each subsection. The final variations of the aperture corrections across the chip were found to be acceptably small and to yield good independent magnitude measurements from the two offset frames.

4.5. Final Magnitude Determination

Before the determination of final magnitudes, the instrumental magnitudes were converted to a standard system, as detailed in §5. Once the calibrated magnitudes were available for each offset image, the final magnitude for each object was determined as follows:

- use the average of the two measurements, unless one measurement lies on a bad pixel, is saturated, or is a limit
- if the object lies on a bad pixel or is saturated in both images, use the average, but flag it as possibly being in error
- if measurement A is a limit, and B is a detection below frame A's limiting magnitude, take the detected value from B as the magnitude
- if measurement A is a limit, and B is a detection above frame A's limiting magnitude, average the two and set the error negative (this last step is done to help mitigate the effects of spurious detections caused by overlooked bad pixels)
- if the final error from the previous steps is greater than 0.333, i.e. the object is fainter than our 3σ detection limit, replace the magnitude of the object with the 3σ magnitude limit of the combined frames, and the error with 0.333

The *average* 3σ magnitude limits in our survey are given for each filter in Table 3. Technically, 3σ detections only require $\sigma < 0.333$, regardless of the object's magnitude, but it is useful to know the average magnitudes to which this limit corresponds. Also, upper magnitude limits for each filter, established by examining the magnitudes of saturated objects, are given in Table 3. Only a handful of saturated objects were found fainter than those limits.

5. Photometric Calibration

Standard stars in M67, M92, and NGC7790 were observed on all nights of both observing runs. Standard magnitudes and color indices were taken variously from Johnson and Sandage

(1955), Eggen and Sandage (1964), Sandage (1966), Schild (1983), Christian et al. (1985), and Odewahn et al. (1992). These data, supplemented with unpublished photometry from A. Porter and L. Davis, are available through the IRAF PHOTCAL on-line library.

Standard star images were reduced in the normal manner for CCD images, using the same domeflats and skyflats used for the field images. Instrumental magnitudes were found for all standard stars using $5''.8$ radius circular apertures, with all other parameters, including the sky annulus size, being the same as used for the field images.

The photometric solution for the *UBVR* filters is independent of that for our two I filters, and is discussed first. In the former case we transform our observed magnitudes to the standard *UBVR* system; in the latter we define a new system for the I filters.

5.1. UBVR Calibration

The IRAF PHOTCAL photometric calibration package was used to interactively solve the following system of equations involving the instrumental magnitudes (lower case), the standard calibrated magnitudes and colors (upper case), and the airmass for the observations in each filter (X_u, X_b, X_v, X_r). The system of equations was solved simultaneously for the zeropoints (u_0, b_0, v_0, r_0), the color coefficients (u_1, b_1, v_1, r_1), and the extinction coefficients (u_2, b_2, v_2, r_2) for each night separately.

$$u = u_0 + u_1 \times (U - B) + u_2 \times X_u + V + (B - V) + (U - B) \quad (1)$$

$$b = b_0 + b_1 \times (B - V) + b_2 \times X_b + V + (B - V) \quad (2)$$

$$v = v_0 + v_1 \times (V - R) + v_2 \times X_v + V \quad (3)$$

$$r = r_0 + r_1 \times (V - R) + r_2 \times X_r + V - (V - R) \quad (4)$$

Not all nights yielded well-defined photometric solutions independently, since typically only

three observations of standard star clusters were made each night. Since most parameters in the solutions had the same values within the errors from night to night, and indeed between the two runs, we decided to adopt the same color terms and extinction coefficients for each observing run and let only the zeropoint in each filter vary. Thus we solved the equations again, this time only for the zeropoint, keeping the other variables fixed at the average values determined from the individual nights' data. The resulting final *UBVR* photometric calibration parameters for both runs are listed in Table 4.

As shown in Table 4, the formal errors associated with the photometric parameters are a few percent at most. However, differences from the base zeropoints were found to exist for most CCD images of the survey fields in both runs, as discussed in §5.3.

5.2. I75 and I86 Calibration

Our magnitude system in the I75 and I86 filters is *defined* by observations of the spectrophotometric standard DA white dwarf Wolf 1346 made on 1990 August 24. The definition and calibration of our system to the AB system are described in detail in this section.

Instrumental magnitudes for Wolf 1346 were determined using a (8''5) radius circular aperture. AB magnitudes for the star were taken from the IRAF ONEDSTDs on-line library, which in the case of Wolf 1346 consists of unpublished data plus data from Oke (1974) for wavelengths redward of 8400 Å. Despite its greater noise, we chose to use the Oke data rather than the data from Massey et al. (1988) because of its better coverage of the 7000-9500 Å wavelength region.

In order to find the effective wavelengths of the filters for this star, the AB magnitudes were converted to fluxes and were convolved with the filter + CCD + telescope system response curves. The effective wavelengths for Wolf 1346 in the I75 and I86 filters are 7430 Å and 8580 Å and

the standard magnitudes of Wolf 1346 are thus defined to be its interpolated AB magnitudes at these wavelengths: I75=12.02 and I86=12.22.

The extinction coefficients at the wavelengths of these filters was calculated in two ways: first by using the standard KPNO extinction curve from the IRAF ONEDSTDs library to find the 'effective extinction coefficient' and second by comparing measurements of the instrumental magnitudes of stars in NGC 7790 made at different airmasses during the same night of the 1990 August run. The extinction coefficients for I75 found by the standard and empirical methods were 0.063 and 0.078 ± 0.014 respectively; and for I86 they were 0.039 and 0.039 ± 0.008 . We chose to adopt the empirical values, but the difference between using the different values would be only a few percent at most, since 94% of our observations were made at airmasses less than 1.4 and 100% at airmasses less than 1.65.

The final step in determining the zeropoints is simply one of plugging in to the equation

$$m_{instr} = m_{AB} + zeropoint + X * airmass \quad (5)$$

which *defines* the zeropoints of the I75 and I86 filters for the 1990 August run. These zeropoints were found to be -22.08 and -21.53, as given in Table 4. Note that no color term was adopted for our two I filters.

In order to obtain the I75 and I86 filter zeropoints for the 1991 April run, the standard stars in the standard fields observed during both runs (M92 and NGC7790) were defined as secondary standards in the I75 and I86 filters as follows. Using the data from 1990 August, equation (5) was solved for m_{AB} for each standard star in each cluster, holding fixed the zeropoints and the extinction coefficients at the values given above. The values of m_{AB} derived from these 1990 August observations were adopted as the magnitudes for these standard stars in our two I filters. The zeropoints for the 1991 April runs were then found by solving the standard photometric transformation equations in the same manner as

equations (1-4) for the *UBVR* filters, with the exception that no color terms were used. Once again, the extinction coefficients were held fixed, because we assumed that the extinction did not change markedly between the two runs, which was certainly the case with the *UBVR* data.

$$i75 = I75 + i75_0 + i75_2 \times X_{i75} \quad (6)$$

$$i86 = I86 + i86_0 + i86_2 \times X_{i86} \quad (7)$$

These zeropoints were found to be -22.03 and -21.48, as given in Table 4. These values are only 5% different from those for 1990 August. Again, as for the *UBVR* filters, some differences from the base zeropoints in were found to exist for most CCD images of the survey fields in both the 1990 August and 1991 April runs, as listed in Table 2.

5.3. Further Empirical Calibration

The photometric calibration derived from the standard stars was checked on the survey fields by calibrating the instrumental magnitudes using only the zeropoint and airmass coefficient at first, i.e. without including the color term. This allowed us to check for any zeropoint shifts between CCD images of the same field and make adjustments to the zeropoints as follows. We plotted the difference between the magnitudes measured for all ‘good’ objects (ones not affected by bad pixels) in the two independent offset frames of each field versus the average of the two magnitudes (hereafter we refer to these as the ‘magnitude difference’ graphs). A typical magnitude difference graph is shown in Figure 3. Figure 3 shows that at bright magnitudes the two measurements agree to within the small (<2%) uncertainty due to limitations of the flat-fielding, etc. It also shows that our bad pixel removal is quite good, with only 2 or 3 objects (out of ~1000) showing differences between the two magnitude measurements large enough to be undisputably due to errors. If the average magnitude difference in a plot like Figure 3 is not zero, one of the frames has been calibrated with

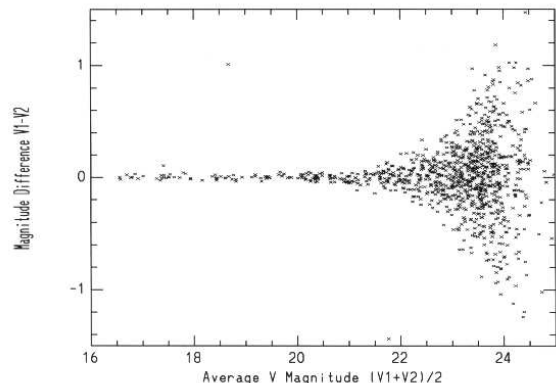


Fig. 3.— A typical magnitude difference graph, in this case from the V images in the 01w field. The x-axis is the average V magnitude measured in the two images for each object, and the y-axis is the difference between the magnitudes measured in the two frames for all ‘good’ objects (ones not affected by bad pixels or focus problems).

an erroneous zeropoint. The magnitude difference graphs are only useful in calculating zeropoint shifts when the same set of objects has been measured; so, in order to measure zeropoint shifts between frames in different fields, we plotted and compared various color-color diagrams as detailed below.

It became apparent from these graphs that empirical corrections to the photometric solutions in most of our fields were necessary in order to bring all fields onto a common system, similar to the practice in astrophotography of calibrating each photographic plate independently. There are many possible explanations for zeropoint differences between fields – the possible presence of light cirrus as noted in our observing logs, as well as night-to-night variations in the atmospheric transparency and extinction, being the most prominent – but for our purposes the exact causes are not relevant. This is because one of the main reasons we calibrate the photometry is to bring all the fields to a common system where

the locus of stellar colors shows as little scatter as possible, which helps us better discriminate candidate quasars from stars. It is not as efficient to search for outliers in each field independently because of the relatively small number of objects that define the stellar locus in each field. That is, a slightly unusual but normal star (e.g. O, B, and A stars at high galactic latitude) will stand out more in the color-color diagrams of each individual field than in the combined diagram of all fields. Strictly speaking, our empirical corrections should be made to the extinction terms in the photometric solution, since they are the most likely to vary. However, it was easier to derive a correction to the zeropoint of each field rather than to the extinction term, so this was done instead. Since the shift needed to align the stellar locus of a given field is fixed, the term used to make that adjustment matters little in practical terms.

The 17n field was adopted as our best field, relative to which all others were adjusted. It showed an average magnitude difference between offset frames of zero in all but the U and B filters, and in those filters it was obvious by inspection and by consulting our observing logs which two frames were affected by light cirrus. Thus we believe that the 17n magnitude calibration is exact to within a few percent. Note, however, that since we have tied our magnitude calibration to this field, any systematic error in the calibration assumed for it will affect all our other fields as well. Since the 17n field was observed in the 1991 April run, all other 1991 April fields had their zeropoints adjusted relative to the 17n field by direct comparison of several color-color diagrams. For both sets of offset frames in each field, color-color diagrams were plotted on an identical scale using the brightest one hundred unsaturated non-bad-pixel objects. Each field's diagrams were compared with those for the 17n field and were shifted by eye in both colors until the best alignment was obtained. The empirically required shift in a given color is simply a

combination of the empirical zeropoint shifts required for the two filters comprising the color. By combining the shifts required for five (independent) colors with the shifts required between frames of the same filter in each field, we are able to determine each field's zeropoint shifts relative to the 17n field to within an additive constant which is the same for all filters. That is, we can determine the relative zeropoint shifts between all filters, but there is still an overall additive constant for the zeropoint in all filters that we cannot determine in the same manner. This additive constant was determined by requiring that all empirical R-band zeropoint shifts be as small as possible relative to the 17n field. This is probably a better estimate than requiring the average zeropoint shift in all filters to be minimized, because the U, B, and V filters will be affected by varying atmospheric extinction more than the R band. For our 1990 August run, we used the fact that the 17s field, which was observed at that time, overlaps with the 17n field. Approximately twenty of the brightest ($R < 20$) objects in the overlap region were used to find the exact shifts between the zeropoints for the two fields by requiring that the average difference between these two independent measures of the magnitudes of these objects be equal to zero. The zeropoints of 17s were adjusted as needed to achieve this, and then the other 1990 August fields were adjusted relative to the 17s field in the same manner as the 1991 April fields were adjusted relative to the 17n field. The average shifts in each filter were less than 5% half the time, and less than 10% in all cases except the R filter in the 1990 August run, where the empirically determined shift was 0.13 magnitudes, or 13%, different from its value calculated by the photometric comparison. While this is uncomfortably high, comparison of color-color plots from different fields shows clearly that our empirical zeropoint shifts achieve the desired result of tightening the stellar locus. Since the empirical shifts in the zeropoints are typically between 5 and 10%, we estimate that the system-

atic uncertainties in our magnitude calibration are at this level.

As a final check, we used bright ($R < 20$) objects, typically two dozen of them, in the overlap regions between the 21-hour and 22-hour fields to confirm our determinations of the zeropoint shifts for the different filters and fields. The magnitudes agreed to within 2σ in all cases. The final zeropoints for each CCD field in both runs are given in Table 2. Note that for all filters in the 01e field and the B filter in the 10e field, only 1 image was obtained. Thus no magnitude difference plot could be constructed, and calibration of the zero points was performed only by color-color diagram comparison. This should not introduce any significant additional uncertainty into the calibration of these fields.

5.4. Photometric Error Analysis And Discussion

We also used the magnitude difference graphs to study the accuracy of the photometric errors determined by the IRAF photometry routines, to ensure that there were no unexpected additional sources of error that had not been taken into account.

The magnitude difference is $d \equiv m_1 - m_2$, where $m_1 \pm \sigma_1$ and $m_2 \pm \sigma_2$ are values of the magnitude of the same object measured from independent CCD frames. Thus the distribution of magnitude differences at any particular magnitude should be given by a gaussian:

$$f(d(m_{avg})) = (1/\sigma_d \sqrt{2\pi}) e^{-[d(m)]^2 / 2\sigma_d^2} \quad (8)$$

where the magnitude $m_{avg} = (m_1 + m_2)/2$ and the sigma of this distribution is $\sigma_d^2(m_{avg}) = \sigma_1^2 + \sigma_2^2$. It is reasonable in most cases to assume $\sigma_1 = \sigma_2$, i.e. that the photometric errors in each CCD frame of a particular filter and field are the same as a function of magnitude. Thus if we measure σ_d , we can find σ from the equation $\sigma = \sigma_d / \sqrt{2}$.

We obtained two different estimates of σ_d from our magnitude difference plots. First, we took

the square of the magnitude difference for every object not affected by a bad pixel, sorted by magnitude, binned them in groups of 50, and calculated the average value of the square of the magnitude difference for each bin. Second, we took the absolute value of the magnitude difference for each object, sorted and binned them as before, and calculated the average absolute value in each bin. This gives us a measure of the mean deviation $\alpha_d = \int |d| f(d) = 0.8\sigma_d$ (Young 1962).

In Figure 4 we plot the photometric errors from the IRAF PHOT routine for all objects in both CCD frames in a representative field and filter and the sigma estimated from the magnitude difference plots in both manners described above. The match is clearly quite good. At the brightest magnitudes we have replaced the photometric errors determined by IRAF with 0.02 if they were originally smaller than this (to be exact, this error should be added in quadrature to all the objects' errors).

In summary, the external errors in our photometry, as estimated from the two independent measurements of the magnitudes of each of our objects, have been shown to be consistent with the internal errors computed according to photon statistics, except for a $\sim 2\%$ additional uncertainty independent of magnitude. This independent check proves that our flatfielding process, aperture correction procedures, and photometry methods are all quite reliable, having inherent limitations of only the aforementioned $\sim 2\%$. As for systematic errors, our stellar locus matches values for stellar colors from the literature to about 5%. An exact match with expected colors is unimportant in terms of outlier selection, but necessary for accurate comparison with other studies and for other uses of the dataset.

6. Astrometry

The final step in the preparation of the catalog was the conversion of CCD (x,y) coordinates (centroids) to right ascension and declination.

We required accuracy to $<0''.5$ because the optical fibers used by the HYDRA instrument for our initial spectroscopy are only $2''.0$ in diameter. The astrometry was performed by A. Porter in the manner briefly outlined here.

The program FINDER (Anderson 1992) was run on each survey field to search for HST Guide Star Catalog (GSC; Taff et al. 1990) stars within the field. There were sometimes less than a dozen or so GSC stars in a field. In these cases we used POSS plates to construct an astrometric grid based on nearby AGK stars. The positions of all the GSC stars in the field, plus a dozen or two anonymous field stars, were then measured on this grid. This served as a check on the GSC astrometry (which was found to be accurate to $<0''.5$ in our fields, adequate for our purposes), and yielded enough stars (between 14-26 for each CCD field) to construct a good astrometric solution. The CCD (x,y) centroids for all these astrometric calibration stars were measured on the first R frames of each field using the IRAF task IMEXAMINE. The astrometric solutions for CCD (x,y) to (RA,dec) conversion in each field were calculated using the program ASTRO (Anderson 1992) and included terms up through a r^2 barrel distortion term. The internal residuals of the solutions ranged from $0''.18$ to $0''.46$, and no significant trends or distortions in the solutions were present. The average positional agreement between stars in the overlap regions of adjacent CCD fields was usually better than $0''.1$ and always better than $0''.4$. The solutions were then used to find the RA and Dec of all objects in the catalog, using the CCD (x,y) positions of the objects as measured from the first R frame of each field.

7. Summary

The final photometrically calibrated catalog of stellar objects in our Deep Multicolor Survey contains 21,375 objects from 0.83° of sky. All objects have positions accurate to $\sim 0''.5$ in each coordinate and magnitudes in six bands whose

errors are consistent with expectations from photon statistics. The production of the catalog is the main result of this paper. From this catalog we would like to isolate as many as possible of the ~ 193 quasars with $B \leq 22.6$ expected in our survey area (Majewski et al. 1993), with a minimum of contamination from stars and other objects. As there are 4,205 objects with $B \leq 22.6$, quasars are outnumbered by a factor of 20:1, and careful candidate selection is obviously necessary. Paper II (Hall et al. 1996) discusses our candidate selection methods and presents initial spectroscopic results and conclusions.

We thank Jeannette Barnes for invaluable assistance (and endless patience) with our IRAF questions, Frank Valdes for essential help with FOCAS, Todd Boroson for providing us with his ‘superflat’ flattening routine, Lindsey Davis for providing us with some unpublished standard-star photometry, the KPNO mountain staff, particularly the telescope operators, for their assistance in observing, and last but definitely not least the KPNO TAC for their allocation of time for this project. PBH acknowledges support from an NSF Graduate Fellowship and a University of Arizona Graduate College Fellowship.

TABLE 1
DEEP MULTICOLOR SURVEY FIELDS

Field	RA (1950.0)	Dec (1950.0)	l(II)	b(II)	Area ^a	E(B-V) ^b
01e	01:00:16	−00:57:52	129.3069	−63.4266	292.4	0.0192
01w	00:59:21	−00:57:55	128.7997	−63.4488	224.9	0.0273
10e	10:34:19	−00:44:40	248.4348	47.1235	286.0	0.0302
14n	13:58:40	−00:37:06	336.7107	57.3613	288.5	0.0283
14s	13:58:40	−00:54:24	336.4456	57.1110	272.8	0.0263
17n	17:14:43	+50:16:47	76.9826	35.5101	266.0	0.0082
17s	17:14:45	+50:00:01	76.6398	35.4963	285.9	0.0093
21e	21:39:57	−04:00:06	51.8119	−39.2835	247.0	0.0243
21w	21:39:01	−04:00:01	51.6505	−39.0849	290.0	0.0203
22e	22:47:04	−02:09:11	68.6033	−51.4310	286.9	0.0542
22w	22:46:07	−02:09:14	68.3400	−51.2595	249.7	0.0492

^aUnits of square arcminutes.

^bCalculated with a program supplied by D. Burstein, using data given in Burstein & Heiles 1978 and Burstein & Heiles 1982.

TABLE 4
PHOTOMETRIC CALIBRATION PARAMETERS

Filter	Color Term	Extinction Coefficient	1991 Base Zeropoint	1991 Average Zeropoint	1990 Base Zeropoint	1990 Average Zeropoint
U	−0.043±0.011	0.530±0.023	−20.64	−20.69	−20.78	−20.71
B	−0.063±0.016	0.275±0.015	−21.71	−21.75	−21.80	−21.74
V	−0.092±0.018	0.113±0.007	−22.45	−22.50	−22.51	−22.46
R	−0.098±0.020	0.087±0.017	−22.06	−22.06	−22.16	−22.03
I75	...	0.078±0.014	−22.03	−22.05	−22.08	−21.99
I86	...	0.039±0.008	−21.48	−21.48	−21.53	−21.45

TABLE 2
OBSERVATIONS

Field	Filter	Frame	Exposure ^a	UT Date	UT Time	Airmass	Seeing($''$)	Zeropoint ^b
01e	U	1.	1350	90/8/24	11:13	1.219	1.60	-20.69
	B	1.	1080	90/8/23	11:00	1.194	1.21	-21.66
	V	1.	540	90/8/23	10:45	1.177	1.10	-22.37
	R	1.	540	90/8/23	11:22	1.216	1.22	-22.02
	I75	1.	540	90/8/23	11:35	1.239	1.28	-21.98
	I86	1.	1080	90/8/24	11:41	1.268	2.03	-21.48
01w	U	1.	1350	90/8/22	10:15	1.170	1.15	-20.85
	U	2.	1350	90/8/22	10:41	1.178	1.24	-20.82
	B	1.	1080	90/8/23	10:09	1.170	1.53	-21.77
	B	2.	1080	90/8/21	10:42	1.175	1.39	-22.79
	V	1.	540	90/8/23	10:31	1.172	1.26	-22.46
	V	2.	540	90/8/21	10:29	1.170	1.14	-22.47
	R	1.	540	90/8/22	9:48	1.181	0.93	-22.02
	R	2.	540	90/8/21	11:04	1.187	1.06	-21.03
	I75	1.	540	90/8/21	10:02	1.173	1.00	-21.96
	I75	2.	540	90/8/21	11:18	1.201	0.99	-21.99
	I86	1.	1080	90/8/22	11:31	1.228	1.39	-21.44
	I86	2.	1080	90/8/22	11:14	1.207	0.95	-21.41
10e	U	1.	1350	91/4/15	6:07	1.338	1.36	-20.74
	U	2.	1350	91/4/15	6:43	1.475	1.37	-20.75
	B	1.	1080	91/4/15	7:10	1.615	1.29	-21.73
	V	1.	540	91/4/14	4:34	1.191	1.41	-22.49
	V	2.	540	91/4/14	4:47	1.195	1.62	-22.48
	R	1.	675	91/4/14	5:02	1.204	1.57	-22.06
	R	2.	675	91/4/14	5:17	1.218	1.66	-22.06
	I75	1.	540	91/4/14	5:32	1.237	1.69	-22.05
	I75	2.	540	91/4/14	5:45	1.258	1.72	-22.05
	I86	1.	1080	91/4/14	6:00	1.302	1.65	-21.48
	I86	2.	1080	91/4/15	5:43	1.244	1.02	-21.50
14n	U	1.	1350	91/4/14	9:08	1.269	2.35	-20.71
	U	2.	1350	91/4/14	9:35	1.336	2.66	-20.77
	B	1.	1080	91/4/15	7:45	1.190	1.10	-21.77
	B	2.	1080	91/4/15	8:07	1.195	1.16	-21.76
	V	1.	540	91/4/14	7:12	1.210	1.54	-22.50
	V	2.	540	91/4/14	6:59	1.225	1.48	-22.50
	R	1.	675	91/4/14	7:26	1.198	1.74	-22.06
	R	2.	675	91/4/14	7:41	1.191	1.70	-22.06
	I75	1.	540	91/4/14	8:09	1.192	1.95	-22.06
	I75	2.	540	91/4/14	7:56	1.189	2.03	-21.06

TABLE 2—*Continued*

Field	Filter	Frame	Exposure ^a	UT Date	UT Time	Airmass	Seeing(^{''})	Zeropoint ^b
14s	I86	1.	1080	91/4/14	8:23	1.202	1.87	-21.48
	I86	2.	1080	91/4/14	8:45	1.225	1.91	-21.48
	U	1.	1350	91/4/16	9:59	1.459	1.69	-20.61
	U	2.	1350	91/4/16	8:45	1.244	1.43	-20.57
	B	1.	1080	91/4/15	7:10	1.208	1.07	-21.77
	B	2.	1080	91/4/17	9:48	1.420	1.88	-21.77
	V	1.	540	91/4/16	8:01	1.196	1.31	-22.30
	V	2.	540	91/4/15	8:51	1.238	1.02	-22.50
	R	1.	675	91/4/16	8:31	1.203	1.40	-21.33
	R	2.	675	91/4/15	9:05	1.263	1.08	-22.06
	I75	1.	540	91/4/17	8:31	1.221	2.12	-22.03
	I75	2.	540	91/4/16	8:31	1.216	1.44	-21.71
	I86	1.	1080	91/4/14	6:00	1.297	1.17	-21.46
	I86	2.	1080	91/4/16	9:35	1.259	1.27	-21.44
17n	U	1.	1350	91/4/16	10:47	1.053	1.57	-20.38
	U	2.	1350	91/4/15	11:01	1.053	1.06	-20.65
	B	1.	1080	91/4/15	10:37	1.056	0.97	-21.73
	B	2.	1080	91/4/16	11:14	1.055	1.40	-21.52
	V	1.	540	91/4/14	10:21	1.066	1.47	-22.50
	V	2.	540	91/4/14	10:36	1.059	1.47	-22.50
	R	1.	675	91/4/14	10:50	1.055	1.34	-22.06
	R	2.	675	91/4/14	11:06	1.053	1.25	-22.06
	I75	1.	540	91/4/14	11:21	1.054	1.20	-22.06
	I75	2.	540	91/4/14	11:33	1.056	1.16	-22.06
	I86	1.	1080	91/4/15	11:29	1.058	0.90	-21.48
	I86	2.	1080	91/4/15	10:14	1.065	0.90	-21.48
	U	1.	1350	90/8/21	5:42	1.289	1.27	-20.76
	U	2.	1350	90/8/24	4:20	1.137	1.26	-20.75
17s	B	1.	1080	90/8/21	4:53	1.169	1.39	-21.79
	B	2.	1080	90/8/23	4:04	1.107	1.44	-21.77
	V	1.	540	90/8/21	4:40	1.139	1.11	-22.49
	V	2.	540	90/8/23	4:26	1.129	1.15	-22.49
	R	1.	540	90/8/23	4:45	1.159	1.21	-22.02
	R	2.	540	90/8/21	5:16	1.205	1.23	-22.05
	I75	1.	540	90/8/21	5:29	1.234	1.06	-21.99
	I75	2.	540	90/8/23	4:57	1.183	1.35	-21.95
	I86	1.	1080	90/8/23	3:41	1.083	1.25	-21.40
	I86	2.	1080	90/8/23	6:10	1.371	1.30	-21.41

TABLE 2—*Continued*

Field	Filter	Frame	Exposure ^a	UT Date	UT Time	Airmass	Seeing($''$)	Zeropoint ^b
21e	U	1.	1350	90/8/24	5:27	1.318	1.71	-20.83
	U	2.	1350	90/8/24	5:53	1.271	1.48	-20.83
	B	1.	1080	90/8/23	5:57	1.274	1.25	-21.81
	B	2.	1080	90/8/24	6:44	1.233	1.78	-21.81
	V	1.	540	90/8/24	7:06	1.234	1.54	-22.50
	V	2.	540	90/8/23	5:42	1.308	1.28	-22.49
	R	1.	540	90/8/24	7:19	1.240	1.57	-22.03
	R	2.	540	90/8/23	6:20	1.251	1.21	-22.02
	I75	1.	540	90/8/24	7:32	1.250	1.38	-22.00
	I75	2.	540	90/8/23	6:33	1.241	1.34	-21.99
	I86	1.	1080	90/8/23	7:13	1.237	1.11	-21.44
	I86	2.	1080	90/8/24	6:21	1.243	1.28	-21.44
21w	U	1.	1350	90/8/21	7:41	1.256	1.86	-20.66
	U	2.	1350	90/8/22	6:23	1.246	1.44	-20.72
	B	1.	1080	90/8/21	6:51	1.234	1.86	-21.77
	B	2.	1080	90/8/22	5:34	1.321	1.19	-21.77
	V	1.	540	90/8/21	6:38	1.242	1.55	-22.49
	V	2.	540	90/8/22	5:21	1.366	1.17	-22.48
	R	1.	540	90/8/22	5:57	1.285	1.02	-22.02
	R	2.	540	90/8/21	7:15	1.234	1.56	-22.06
	I75	1.	540	90/8/21	7:28	1.239	1.52	-22.01
	I75	2.	540	90/8/22	6:09	1.266	1.00	-21.99
	I86	1.	1080	90/8/21	6:08	1.291	1.64	-21.48
	I86	2.	1080	90/8/22	6:50	1.233	1.54	-21.46
22e	U	1.	1350	90/8/24	8:27	1.218	1.80	-20.62
	U	2.	1350	90/8/24	8:54	1.248	1.38	-20.66
	B	1.	1080	90/8/24	9:42	1.349	2.32	-21.68
	B	2.	1080	90/8/23	8:30	1.215	1.06	-21.69
	V	1.	540	90/8/23	8:15	1.206	1.09	-22.44
	V	2.	540	90/8/24	10:04	1.407	1.86	-22.45
	R	1.	540	90/8/23	8:51	1.230	0.98	-22.07
	R	2.	540	90/8/24	10:17	1.461	2.05	-22.00
	I75	1.	540	90/8/23	9:04	1.246	1.11	-22.01
	I75	2.	540	90/8/24	10:30	1.522	1.83	-22.03
	I86	1.	1080	90/8/24	9:21	1.293	1.63	-21.48
	I86	2.	1080	90/8/23	9:44	1.343	1.09	-21.46

TABLE 2—*Continued*

Field	Filter	Frame	Exposure ^a	UT Date	UT Time	Airmass	Seeing('')	Zeropoint ^b
22w	U	1.	1350	90/8/24	7:59	1.206	1.57	-20.52
	U	2.	1350	90/8/22	9:06	1.257	1.23	-20.46
	B	1.	1080	90/8/22	8:18	1.207	1.24	-21.62
	B	2.	1080	90/8/21	9:09	1.250	1.59	-21.67
	V	1.	540	90/8/21	8:55	1.227	1.52	-22.45
	V	2.	540	90/8/22	8:05	1.205	1.12	-22.42
	R	1.	540	90/8/22	8:40	1.217	1.01	-22.02
	R	2.	540	90/8/21	9:40	1.302	1.45	-22.04
	I75	1.	540	90/8/22	8:53	1.229	1.07	-21.98
	I75	2.	540	90/8/21	9:53	1.334	1.54	-22.00
	I86	1.	1080	90/8/23	7:47	1.207	1.11	-21.47
	I86	2.	1080	90/8/22	7:14	1.234	1.57	-21.47

^aUnits of seconds.^bSee §5.3.TABLE 3
AVERAGE MAGNITUDE LIMITS

Filter	Threshold Magnitude	5 σ Limiting Magnitude ^a	3 σ Limiting Magnitude ^b	Upper Limit Magnitude	G(m _{5σ}) ^c
U	21.0	22.8	23.45	16.0	25.2%
B	21.5	23.8	24.30	16.5	22.2%
V	21.0	23.5	24.00	16.5	27.8%
R	20.0	23.0	23.50	16.5	33.0%
I75	20.0	22.4	23.05	16.0	19.5%
I86	19.5	22.1	22.70	16.0	21.5%

^aAlso 90% completeness magnitude.^bAlso 50% completeness magnitude.^cThe percentage of misclassified galaxies in the stellar object catalog at the 5 σ limiting magnitude.

REFERENCES

- Anderson, E., 1992, Finder and Astro on the VMS VAX, Kitt Peak National Observatory, Central Computer Services, Tucson AZ
- Burstein, D., & Heiles, C. 1978, *ApJ*, 225, 40
- Burstein, D., & Heiles, C. 1982, *AJ*, 87, 1165
- Christian, C. A., Adams, M., Barnes, J. V., Butcher, H., Hayes, D. S., Mould, J. R., & Siegel, M. 1985, *PASP*, 97, 363
- Crampton, D., Le Fevre, O., Lilly, S. J., & Hammer, F. 1995, *ApJ*, in press
- Eggen, O., & Sandage, A. 1964, *ApJ*, 140, 130
- Fall, S. M., & Pei, Y. C. 1993, *ApJ*, 402, 479
- Giallongo, E., & Vagnetti, F. 1992, *ApJ*, 396, 411
- Griffiths, R. E., et al. 1994, *ApJ*, 437, 67
- Gullixson, C. A. 1992, in *Astronomical CCD Observing and Reduction Techniques*, ed. S. B. Howell (ASP: San Francisco), 130
- Haehnelt, M. G., & Rees, M. J., 1993, *MNRAS*, 263, 168
- Hall, P. B., Osmer, P. S., Green, R. F., Porter, A. C., & Warren, S. J. 1996, *ApJ*, submitted
- Hewett, P. C., Foltz, C. B., & Chaffee, F. C. 1993, *ApJ*, 406, L43
- Im, M., Casertano, S., Griffiths, R. E., Ratnatunga, K. U., & Tyson, J. A. 1995, *ApJ*, 441, 494
- Johnson, H. L. 1966, *ARAA*, 4, 193
- Johnson, H., & Sandage, A. 1955, *ApJ*, 121, 616
- Kaiser, N., & Tribble, P. 1991, in *The Space Distribution of Quasars*, ed. D. Crampton (ASP: San Francisco), 304
- Katz, N., Quinn, T., Bertschinger, E., & Gelb, J. M. 1994, *MNRAS*, 270, L71
- Koo, D. C., & Kron, R. G. 1988, *ApJ*, 325, 92
- Liu, C. T., Green, R. F., Hall, P. B., & Osmer P. S. 1996, in preparation
- Loeb, A. 1993, *ApJ*, 403, 542
- Majewski, S. R., Munn, J. A., Kron, R. G., Bershad, M. A., Smetanka, J. J., & Koo, D. C. 1993, in *The Evolution of Galaxies and Their Environment*, ed. Hollenbach, D. A., Thronson, H. A., & Shull, J. M., NASA Conference Proceedings, 9
- Massey, P., Strobel, K., Barnes, J. V., & Anderson, E. 1988, *ApJ*, 328, 315
- McLeod, B. A., & Rieke, M. J., 1995, *ApJ*, in press
- Miller, L., Goldschmidt, P., La Franca, F., & Cristiani, S., 1993, in *Observational Cosmology*, eds. G. Chincarini, A. Iovino, T. Maccacaro, & D. Maccagni (ASP: San Francisco), 614
- Neuschaefer, L. W., & Windhorst, R. A. 1995, *ApJ*, 439, 14
- Nusser, A., & Silk, J. 1993, *ApJ*, 411, L1
- Odewahn, S. C., Bryja, C., & Humphreys, R. M. 1992, *PASP*, 104, 553
- Oke, J. B. 1974, *ApJS*, 27, 21
- Oke, J. B., & Gunn, J. E. 1983, *ApJ*, 266, 713
- Osmer, P. S. 1982, *ApJ*, 253, 28
- Osmer, P. S., Green, R. F., Hall, P. B., & Warren, S. J. 1996, *ApJ*, in preparation
- Reid, N., & Majewski, S. R. 1993, *ApJ*, 409, 635
- Roche, N., Shanks, T., Metcalfe N., & Fong, R. 1993, *MNRAS*, 263, 360
- Sandage, A. 1966, *ApJ*, 143, 313
- Schild, R. E. 1983, *PASP*, 95, 1021

- Schmidt, M., & Green, R. F. 1983, *ApJ*, 269, 352
- Schmidt, M., Schneider, D. P., & Gunn, J. E. 1995, *AJ*, 110, 68
- Smetanka, J. J. 1993, in *The Evolution of Galaxies and Their Environment*, ed. Hollenbach, D. A., Thronson, H. A., & Shull, J. M., NASA Conference Proceedings, 19
- Steidel, C. C., & Sargent, W. L. W. 1992, *ApJS*, 80, 1
- Stetson, P. B. 1990, in *The Formation and Evolution of Star Clusters*, ed. Janes, K. (ASP: San Francisco), 88
- Taff, L. G., Lattanzi, M. G., Bucciarelli, B., Gilmozzi, R., McLean, B. J., Jenkner, H., Laidler, V. G., Lasker, B. M., Shara, M. M., & Sturch, C. R., 1990, *ApJ*, 353, L45
- Turner, E. L. 1991, *AJ*101, 5
- Valdes, F. 1982a, *FOCAS User's Manual*, Kitt Peak National Observatory, Central Computer Services, Tucson AZ
- Valdes, F. 1982b, *The Resolution Classifier*, in *Instrumentation in Astronomy IV*, SPIE Proceedings, Vol. 331
- Warren, S. J., Hewett, P. C., Irwin, M. J., & Osmer, P. S. 1991a, *ApJS*, 76, 1
- Warren, S. J., Hewett, P. C., & Osmer, P. S. 1994, *ApJ*, 421, 412
- Yee, H. K. C., & Ellingson, E., 1993, *ApJ*, 411, 43
- Young, H. D., 1962, *Statistical Treatment of Experimental Data* (New York: McGraw-Hill), p. 73

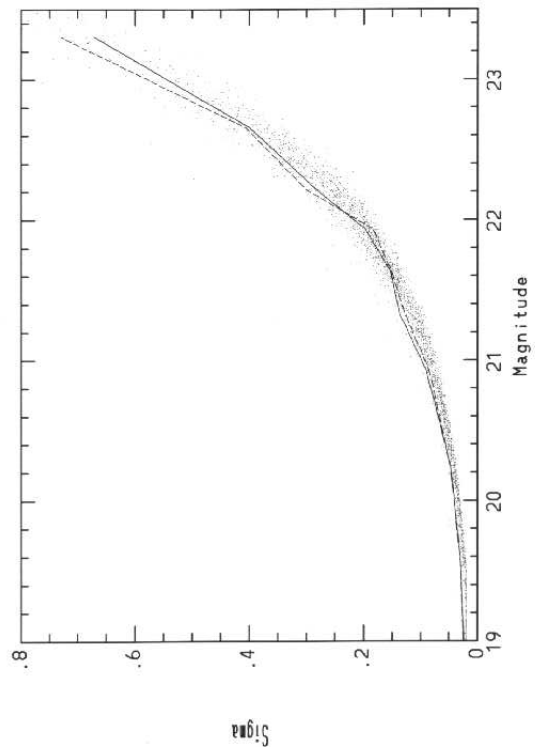


Fig. 4.— Formal photometric errors vs. errors estimated from the magnitude difference plots like that shown in Figure 3. The points are the photometric errors from the IRAF ‘phot’ routine for all objects in both CCD frames in the 21w field, I8600 filter. The dashed line is the sigma estimated from the average square of the magnitude difference for every 50 objects, while the connected line is the sigma estimated for every 50 objects using the average absolute value of the magnitude difference. The match is clearly quite good at all magnitudes.